http://dx.doi.org/10.1097/mm9.0000000000000034

MedMat

Original Research

OPEN

Zinc gallate nanoclusters-mediated enhanced metalloptosis in melanoma

Ran Ma[a], Jiajia Liu[a], Zi Mei[b], Yanglong Hou[a,c,d], Shuren Wang[a,*]

Abstract

As one of the most malignant tumors, metastatic melanoma essentially requires the regulation of the lysosomal cation channel, transient receptor potential mucolipin channel 1 (TRPML1), which is also involved in the participation of various ions, especially zinc ions. This perfectly aligns with the advanced therapeutic approach based on nanomaterials, because nanomaterials can easily integrate multiple metal elements to disrupt the internal homeostasis of various ions, eventually inhibiting the cell growth of metastatic melanoma. Hence, based on our previously proposed metalloptosis strategy, herein, zinc gallate-based nanoclusters (ZGOCs) containing both zinc and gallium were developed, capable of inducing metalloptosis. Responded to a weak-acid tumor microenvironment, ZGOCs could effectively release gallium ions that triggered ferroptosis through depleting glutathione and increasing lipid peroxidation levels. Moreover, the released zinc ions co-treated with ML-SA5, a TRPML-specific agonist, further promoted lysozincrosis. In addition, ZGOCs exhibited rechargeable afterglow luminescence, which facilitated in vivo clearer diagnostic images with high contrast for more accurate detection of tumor boundaries. Collectively, ZGOCs in combination with ML-SA5 significantly suppressed tumor growth with favorable biosafety, providing a promising metalloptosis-based strategy for the treatment of metastatic melanoma.

Keywords: Ferroptosis, Lysozincrosis, Melanoma, Metalloptosis, Synergistic therapy

1. Introduction

Compared to primary melanoma, metastatic melanoma often calls for more efficient and precise treatment due to the higher mortality rates and more severe suffering. Therefore, identifying appropriate targets is particularly important for the precise treatment of metastatic melanoma[1]. Dependent on the pathological features of metastatic melanoma, the abnormality of lysosomes is crucial to promote the development of metastatic melanoma, which is also regulated by the lysosomal cation channel, transient receptor potential mucolipin channel 1 (TRPML1)[2]. TRPML1 is a kind of permeable cation channel involved in various metal ions, such as calcium ions (Ca^{2+}), ferrous ions (Fe^{2+}), and zinc ions (Zn^{2+})[3]. Expectedly, disrupting the homeostasis of these metal ions is one of the effective strategies for suppressing metastatic melanoma. For example, TRPML1-specific synthetic agonists trigger lysosomal Zn^{2+} release, leading to rapid metastatic melanoma cell death, while curcumin targets Ca^{2+} signaling pathways, enhancing endoplasmic reticulum stress and killing melanoma cells[4–6]. However, the ion homeostasis disruption effects induced by these small molecule drugs are relatively limited, and they often face significant challenges in clinical applications, such as short circulation times, poor targeting specificity, and limited functional versatility, which restrict their overall efficacy[7]. These limitations highlight the need for more advanced therapeutic approaches to improve treatment outcomes. Nanomaterials (NMs) possess unique physicochemical properties that allow for the integration of targeted delivery, controlled release, and multimodal therapeutic functionalities, potentially enhancing the synergistic effects of traditional therapies[8–10]. Hence, NMs-mediated advanced treatments can effectively overcome the above-mentioned limitations by incorporating multiple metal elements into a single carrier, aligning with the principles of the metalloptosis strategy[11].

Metalloptosis is our newly-proposed concept that describes programmed cell death (PCD) induced by metal ions, including well-established forms such as ferroptosis, cuproptosis, and calcium overload, which are closely linked to the levels of iron (Fe), copper (Cu), and calcium (Ca) ions in cells[11]. Additionally, other metal ions, such as zinc (Zn), manganese (Mn), and sodium (Na), can also trigger PCD through more general signaling pathways, and these processes are collectively categorized under metalloptosis[11]. Metalloptosis presents several advantages, including high specificity, reduced resistance, and diverse mechanisms of action, which have generated increasing interest in its potential application in cancer therapy[12,13]. Several design principles are essential for the development of NMs in this emerging field[11]. These include rational metal selection based on valence-dependent redox activity and cytotoxicity, and incorporation of controlled-release mechanisms responsive to tumor-specific characteristics such as pH, reactive oxygen species (ROS), and glutathione (GSH)[14]. For example, by engineering iron-based nanoparticles (NPs) into smart nanocapsules, they could be programmed to respond to acidic or hyperthermic stimuli, thereby enabling precise activation of the ferroptosis pathway[15]. However, previously reported NMs that induce metalloptosis still have some inevitable limitations. For instance, ferroptosis, a form of lipid peroxidation (LPO)-dependent, iron-driven PCD,

[a]*School of Materials Science and Engineering, Peking University, Beijing, China,* [b]*Department of Infection and Immunity, Luxembourg Institute of Health, Esch-sur-Alzette, Luxembourg,* [c]*School of Materials, Shenzhen Campus of Sun Yat-sen University, Shenzhen, China,* [d]*State Key Laboratory of Optoelectronic Materials and Technologies, Sun Yat-Sen University, Guangzhou, China.*

**Corresponding author: Address: Shuren Wang. School of Materials Science and Engineering, Peking University, Beijing, 100871, China. E-mail address: shurenwang_wsr@pku.edu.cn (S. Wang).*

Supplemental Digital Content is available for this article.

MedMat (2026) 3:2

Received: 4 October 2025; Accepted 28 November 2025

Published online 30 December 2025

exhibits high specificity for cancer cells with aberrant iron metabolism or compromised antioxidant defenses[16,17]. However, the effectiveness of ferroptosis-inducing NMs may be hindered by their short shelf life, as they tend to aggregate, which can reduce their stability and performance[18]. To address this issue and ensure consistent therapeutic efficacy, it is crucial to synthesize NMs with stable particle sizes, uniform morphology, and good biocompatibility, thereby maximizing their potential to induce ferroptosis effectively. Moreover, the release of lysosomal Zn ions can trigger a nonapoptotic cell death pathway in melanoma cells, referred to as "lysozincrosis"[4]. In metastatic melanoma cells, the expression of TRPML1 is significantly upregulated. Treatment of these cells with TRPML1-specific synthetic agonists (ML-SAs, such as ML-SA5) can rapidly induce lysosome-dependent, Zn^{2+}-mediated necrotic cell death, accompanied by mitochondrial dysfunction and adenosine triphosphate (ATP) depletion[4]. While lysozincrosis shows promising effects against metastatic melanoma cells, further investigation into its mechanisms and interactions with other forms of metalloptosis is crucial for enhancing its therapeutic potential.

Herein, we synthesized a kind of zinc gallate-based NPs containing both gallium (Ga) ions and zinc ions to enhance metalloptosis for metastatic melanoma therapy. By introducing trace amounts of Cr^{3+}, the resulting $ZnGa_2O_4$:Cr (simplified as ZGO) NPs also exhibited a persistent near-infrared (λ = 650–750 nm) afterglow emission, which is advantageous for high-sensitivity tumor imaging without background fluorescence interference[19]. Furthermore, by assembling individual ZGO NPs into well-defined clusters (ZGOCs), we obtained nanostructures with uniform morphology, optimized size, and favorable surface charge, thereby promoting prolonged blood circulation and enhanced tumor accumulation[20]. In addition, such clustering also improved the persistent luminescence (PL) of ZGOCs to a certain extent, further strengthening their potential for more precise imaging-guided cancer therapy with a high signal-to-noise ratio. After being engulfed by melanoma cells, ZGOCs were effectively degraded and released gallium ions and zinc ions, which induced ferroptosis and promoted lysozincrosis, respectively. Specifically, ZGOCs administration resulted in obvious GSH depletion and LPO increment, triggering ferroptosis. Besides, the co-treatment of ZGOCs and ML-SA5, a TRPML-specific agonist, significantly reduced cellular ATP levels, subsequently enhancing zinc ions-mediated lysozincrosis. In summary, we presented an enhanced metalloptosis strategy of synergistical ferroptosis and lysozincrosis based on ZGOCs, holding promise for the efficient treatment of melanoma in the future (Figure 1).

2. Experimental

2.1 Materials and reagents

All purchased information of materials and reagents were as follows: $Zn(NO_3)_2{\cdot}6H_2O$ (XILONG Scientific Company); $Ga(NO_3)_3{\cdot}xH_2O$ and Sodium dodecylsulfate (J&K Chemicals); $Cr(NO_3)_3{\cdot}9H_2O$ (Aladdin); ML-SA5 (Target Molecule Corp.); NaOH (Energy Chemical); Absolute ethanol and Cyclohexane (Beijing Tong Guang Fine Chemical Company); Oleic acid (OA, Alfa Aesar); 5-FAM (Xi'an Ruixi Biological Technology Company); Deferoxamine (DFO) mesylate (Abcam); Chloroquine (CQ), Z-VAD-fmk and Necrostatin-1 (HARVEYBIO); Lipid peroxide colorimetric assay kit (Elabscience Biotechnology Co., Ltd.); Calcein-AM/PI double stain kit and Reduced glutathione content assay kit (Beijing Solarbio Science & Technology Co., Ltd.); ATP content assay kit (Shanghai Acmec Biochemical Technology Co., Ltd.); N,N,N,N-Tetrakis(2-pyridylmethyl)-ethylenediamine (Shanghai Macklin Biochemical Technology Co., Ltd.); DAPI and ROS assay kit (Beyotime); Cell counting kit-8 (CCK-8) (LABLEAD); Dulbecco' s modified Eagle medium (DMEM), PBS and trypsin-EDTA (Shanghai XP Biomed Ltd.); fetal bovine serum (FBS) and penicillin-streptomycin (Invitrogen). The following primary antibodies were purchased from

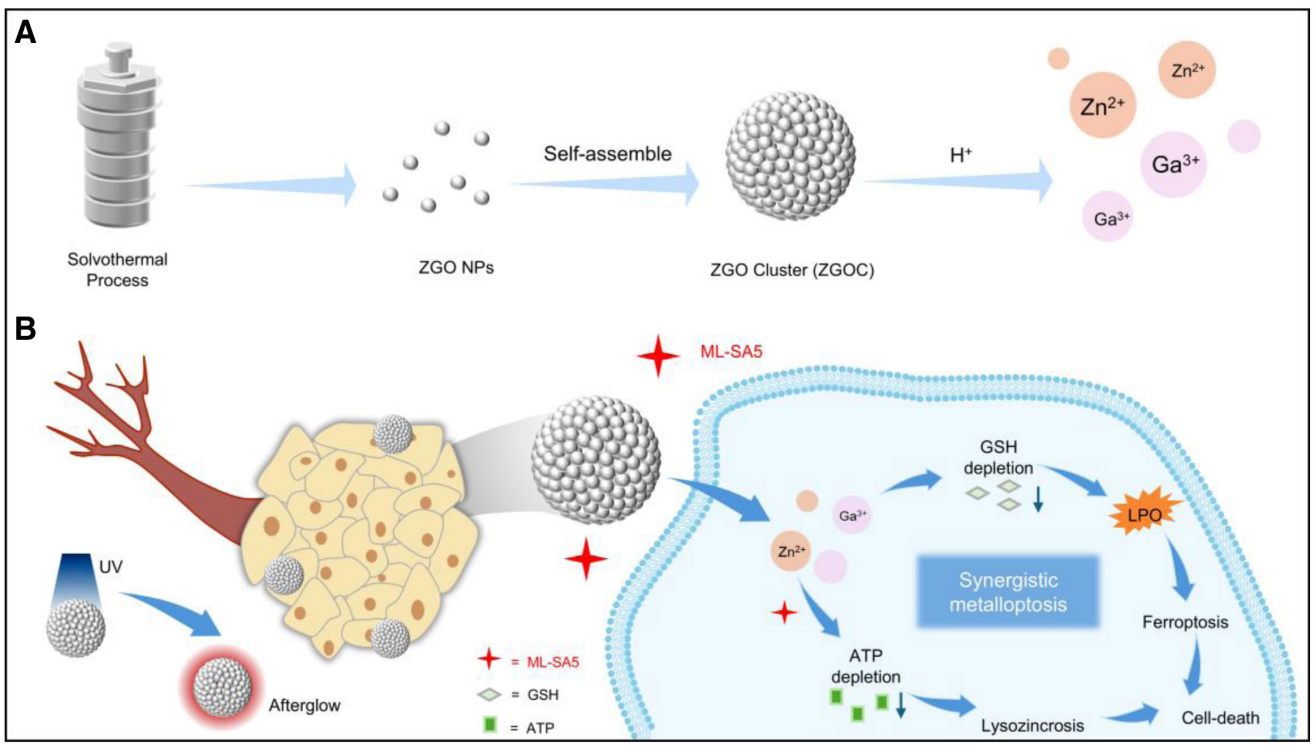

Figure 1. Schematic illustration of ZGOCs-induced metalloptosis for melanoma therapy. (A) Preparation of ZGOCs. (B) Proposed mechanism of ZGOCs in combination with ML-SA5 in melanoma cells, enabling synergistic metalloptosis induction and afterglow-based imaging applications. ZGOCs, zinc gallate-based nanoclusters.

HUABIO: Beta Actin (1:5000, EM21002), glutathione peroxidase 4 (GPX4) (1:1000, ET1706-45).

2.2 Methods

2.2.1 Preparation of ZGO NPs and ZGOCs

ZGO NPs were synthesized as follows. Typically, 0.297 g of $Zn(NO_3)_2 \cdot 6H_2O$, 0.511 g of $Ga(NO_3)_3 \cdot xH_2O$, and 1.6 mg of $Cr(NO_3)_3 \cdot 9H_2O$ were dissolved in a mixture formed by 0.6 g of NaOH, 6 mL of OA, 8 mL of deionized water, and 18 mL of ethanol under vigorous stirring. The mixture was then transferred to a 50 mL teflon-lined autoclave and heated at 210 °C for 16 h. After cooling to room temperature, the resulting ZGO NPs were precipitated, isolated by centrifugation, washed alternately with ethanol and cyclohexane for 3 cycles, and finally redispersed in cyclohexane for further synthesis.

ZGOCs were synthesized with some modifications by following a previous protocol[21]. Sodium dodecylsulfate (28 mg) was first dissolved in 10 mL of deionized water. Then, 10 mg of ZGO NPs in 1 mL of cyclohexane was added to the solution. The mixture was emulsified using ultrasonic treatment, and the cyclohexane was evaporated by heating at 70 °C with vigorous stirring for 4 hours, assembling the ZGO NPs into ZGOCs. After cooling to room temperature, the products were collected, purified by repeated centrifugation, and redispersed. The final products were stored in water or PBS for future use.

2.2.2 Characterization of ZGO NPs and ZGOCs

The morphology and element mapping of the ZGO NPs and ZGOCs were examined using transmission electron microscopy (TEM, FEI Tecnai T20, HT-7700, 200 kV). X-ray diffraction (XRD) patterns were obtained with a Rigaku DMAX-2400 diffractometer using Cu Kα radiation (λ = 0.15405 nm). The hydrodynamic sizes of ZGOCs were measured with a dynamic light scattering analyzer (Zetasizer Nano ZS-90, Malvern, England). Fourier transform infrared (FT-IR) spectra were collected by a Bruker Frontier spectrometer (VERTEX 70v). PL observation of ZGO NPs and ZGOCs was measured using an *In Vivo* Imaging System (IVIS Luminn XRMS, Series III).

2.2.3 Degradation behavior analysis

ZGOCs were dispersed in PBS solutions with pH levels of 7.4, 6.5, and 5.4, then placed in a 37 °C shaker at 150 rpm for 8 h. Afterward, 50 µL of the solution was placed on a copper grid for TEM analysis.

2.2.4 Cell culture and cell viability study

NIH3T3 and B16F10 cell lines were obtained from the Cancer Institute and Hospital of the Chinese Academy of Medical Sciences. NIH3T3 and B16F10 cell lines were cultured in DMEM medium containing 10% FBS and 1% penicillin-streptomycin in a humidified environment at 37 °C with 5% CO_2.

For the cell viability study, cells were incubated with varying concentrations of ZGOCs or ML-SA5 in DMEM at 37 °C and 5% CO_2 for 24 h. Cell viability was then assessed using the CCK-8 assay. Additionally, the protective effect of different cell death inhibitors on ZGOCs-treated B16F10 cells was evaluated by incubating the cells with different inhibitors for 24 h, followed by cell viability measurement using the CCK-8 assay.

2.2.5 In vitro ferroptosis assay

To evaluate the ability of ZGOCs to induce ferroptosis, B16F10 cells were incubated and treated with either PBS (control) or ZGOCs. The cells were then collected to measure GSH and LPO levels using commercial kits. ROS levels were assessed with a ROS assay kit, and fluorescence images were captured using fluorescence microscopy.

2.2.6 Animal experiments

Female C57BL/6J mice (8 weeks old) were purchased from Beijing Vital River Laboratory Animal Technology Co., Ltd. All animal experiments were conducted following guidelines approved by the Institutional Animal Care and Use Committee of Peking University, with an assigned approval number: MSE-HouYL-1.

2.2.7 In vivo tumor treatment effect evaluation

Subcutaneous melanoma-bearing C57BL/6J mice were randomly divided into 4 groups: (1) control (saline), (2) ML-SA5, (3) ZGOCs, and (4) ZGOCs + ML-SA5. ZGOCs (10 mg/kg, 200 µL) were injected intravenously, and ML-SA5 was administered intraperitoneally (5 mg/kg), following the timeline shown in Figure 6A. During the treatment period, tumor volumes and body weights were monitored and recorded at specific time points. After treatment, tumors from each group were collected for histopathological analysis, including hematoxylin and eosin (H&E) staining and immunohistochemical (IHC) analysis.

2.2.8 Histological evaluation

The isolated major organs and tumors were fixed with 4% paraformaldehyde. The tissues were embedded in paraffin and sectioned at 5 mm; H&E staining was performed for histological evaluation. The slides were observed under an optical microscope.

2.2.9 Immunohistochemistry

The paraffin sections of tumor tissues in mice were prepared at the end of the treatment. IHC was performed as described previously[22]. Primary antibodies used for IHC staining included anti-Ki-67 (1:500; Bioss, BSM-52455R) and anti-Solute Carrier Family 7 Member 11 (SLC7A11, also known as xCT) (1:200; Affinity Biosciences, DF12509).

2.2.10 Statistical analysis

Results in this work were presented as mean values ± SD or mean values ± SEM, which were described in the corresponding figure legends. The student's two-tailed nonpaired *t*-test was used to determine significance between treatment and control groups in all experiments. $P < 0.05$ was considered statistically significant; $^{*}P < 0.05$, $^{**}P < 0.01$, $^{***}P < 0.001$, and $^{****}P < 0.0001$. NS, not significant.

3. Result and discussion

3.1 Synthesis and characterization

ZGO NPs were synthesized using a simple solvothermal liquid-solid-solution method, involving the reaction of metal salts in a mixture of NaOH, ethanol, and OA. Due to the presence of OA ligands on the surface, the resulting ZGO NPs could be well-dispersed in nonpolar solvents such as cyclohexane (CYH), which enabled the formation of clusters in subsequent steps. TEM images demonstrated that ZGO NPs exhibited excellent dispersion and uniformity, with a particle size of approximately 10 nm (Figure 2A, B).

Subsequently, the organic phase (CYH) containing OA-modified ZGO NPs was mixed with an aqueous solution containing the surfactant sodium dodecylsulfate (SDS) to form an oil-in-water microemulsion via ultrasonic treatment. The

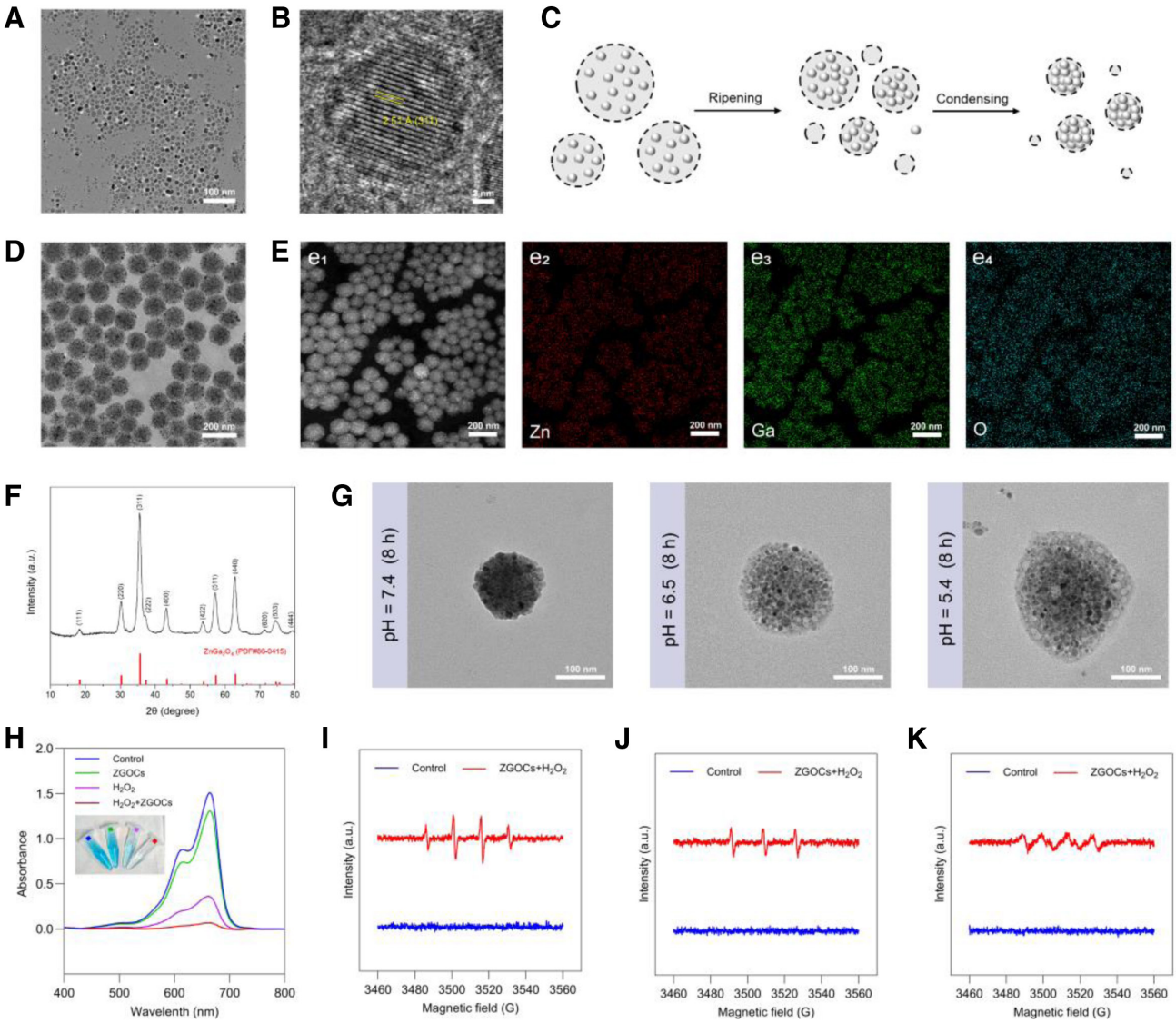

Figure 2. Preparation and characterization of ZGOCs. (A) TEM characterization of the ZGO NPs. (B) HR-TEM image of ZGO NPs. (C) Illustration of the forming process of ZGOCs through a microemulsion-based approach. (D) TEM image and (E) EDS mappings of ZGOCs. (F) XRD pattern of ZGOCs. (G) TEM images of ZGOCs after incubation in PBS with pH values of 7.4, 6.5, and 5.4 (37 °C) for 8 hours. (H) UV-Vis absorbance spectra and photo (inset) of MB solutions with different treatments. (I–K) EPR spectra of ZGOCs treated with H_2O_2 in the presence of different spin-trapping agents. EDS, Energy dispersive spectrometry; EPR, electron paramagnetic resonance; MB, methylene blue; NP, nanoparticles; TEM, transmission electron microscopy; XRD, X-ray diffraction; ZGO, $ZnGa_2O_4$; ZGOCs, zinc gallate-based nanoclusters.

low-boiling organic solvent CYH was then evaporated through vigorous stirring, successfully yielding ZGOCs. During this process, emulsions formed by ultrasonication underwent ripening, where solvent-swollen micelles were generated. As the solvent evaporated, clusters and SDS micelles formed (Figure 2C)[21]. TEM images revealed that the assembled ZGO clusters maintained a uniform morphology (Figure 2D). It is important to note that the feeding ratio of ZGO NPs during synthesis was critical. A reduced amount of ZGO NPs resulted in many unassembled monomers in the product (Supplementary Figure S1, https://links.lww.com/MEDMAT/A7). The hydrophobic van der Waals interactions between the alkyl chains of SDS surfactant in the aqueous phase and the alkane chains of OA ligands on ZGO NPs surface (Supplementary Figure S2, https://links.lww.com/MEDMAT/A7) contributed to the good water solubility of the obtained ZGOCs[21]. The hydrodynamic diameter of ZGOCs in water was approximately 100 nm, with a polydispersity index of 0.075 (Supplementary Figure S3a, https://links.lww.com/MEDMAT/A7), indicating their excellent dispersibility and uniformity, which was advantageous for subsequent biological applications. The zeta potential of ZGOCs was measured to be –19 mV (Supplementary Figure S3b, https://links.lww.com/MEDMAT/A7), suggesting their favorable long-circulating behavior *in vivo*[23]. Energy dispersive spectrometry mapping and X-ray photoelectron spectroscopy together confirmed the presence of Zn, Ga, and O in ZGOCs (Figure 2E and Supplementary Figure S4, https://links.lww.com/MEDMAT/A7). The lack of Cr in the elemental mapping analysis arises from its trace doping concentration that could not be detected by the instrument[24]. The XRD patterns further confirmed the presence of a pure zinc gallate phase in ZGOCs (Figure 2F).

The degradation behavior of ZGOCs was studied by dispersing them in PBS with different pH values at 37 °C environments, simulating specific physiological conditions (Figure 2G). Remarkably, ZGOCs were stable at pH 7.4, indicating strong stability under physiological conditions, consistent with the results shown in Supplementary Figure S3c, https://links.lww.com/MEDMAT/A7. However, at pH 6.5 and 5.4, ZGOCs gradually

degraded within 8 hours, accompanied by an increase in particle size and the release of ZGO NPs, demonstrating an acid-sensitive degradation process. Such pH-responsive degradation not only ensures the structural stability of ZGOCs during systemic circulation but also facilitates the release of active zinc and gallium ions in the acidic TME, which is expected to enhance their catalytic reactivity. Guided by this rationale, we next evaluated the catalytic activities of ZGOCs. Methylene blue (MB) was employed as a dye indicator to assess the generation of ROS. As shown in the UV-vis absorbance spectra (Figure 2H), the treatment of MB with ZGOCs in the presence of hydrogen peroxide (H_2O_2) led to the most pronounced decrease in absorbance compared with other groups, indicating the superior catalytic performance of ZGOCs. Furthermore, electron paramagnetic resonance spectroscopy confirmed the production of multiple ROS species, including hydroxyl radicals, superoxide anions, and singlet oxygen, when ZGOCs were incubated with H_2O_2 in the presence of different spin-trapping agents (Figure 2I–K).

3.2. In vitro *anticancer activity and mechanism*

We chose metastatic melanoma cell lines B16F10 and investigated the cellular uptake behavior of ZGOCs. After incubating 5-FAM-labeled ZGOCs with B16F10 cells for 8 hours, significant fluorescence was observed in the cells using confocal laser scanning microscopy, confirming efficient intracellular internalization (Figure 3A). Additionally, cellular bio-TEM images (Figure 3B) further supported the phagocytosis of ZGOCs by tumor cells, laying the foundation for subsequent metalloptosis-based therapy.

To assess the cytotoxicity of ZGOCs on B16F10 cells, we used the CCK-8 assay. After 24 h of incubation, ZGOCs exhibited a concentration-dependent cytotoxic effect on B16F10 cells (Figure 3C). Notably, no significant toxicity of ZGOCs was observed in normal cells NIH3T3 (Supplementary Figure S5, https://links.lww.com/MEDMAT/A7). To further investigate the specific mechanism of cell death, various cell death inhibitors were selected for validation. Specifically, the apoptosis inhibitor Z-VAD-fmk (Z-VAD), the necroptosis inhibitor necrostatin-1 (Nec-1), the autophagy inhibitor CQ, and the lysosomal inhibitor N,N,N,N-Tetrakis(2-pyridylmethyl)-ethylenediamine (a Zn^{2+} chelator) showed no rescue effects on ZGOCs-induced cell death. However, the ferroptosis inhibitor DFO reversed the cytotoxic effect of ZGOCs to a certain extent, indicating that ZGOCs induced B16F10 cell death primarily through ferroptosis. This finding was also consistent with recent research, which suggested that gallium ions could also induce oxidative stress and trigger ferroptosis via indirect mechanisms[25]. We further measured GSH levels and the deactivation of GSH-related GPX4

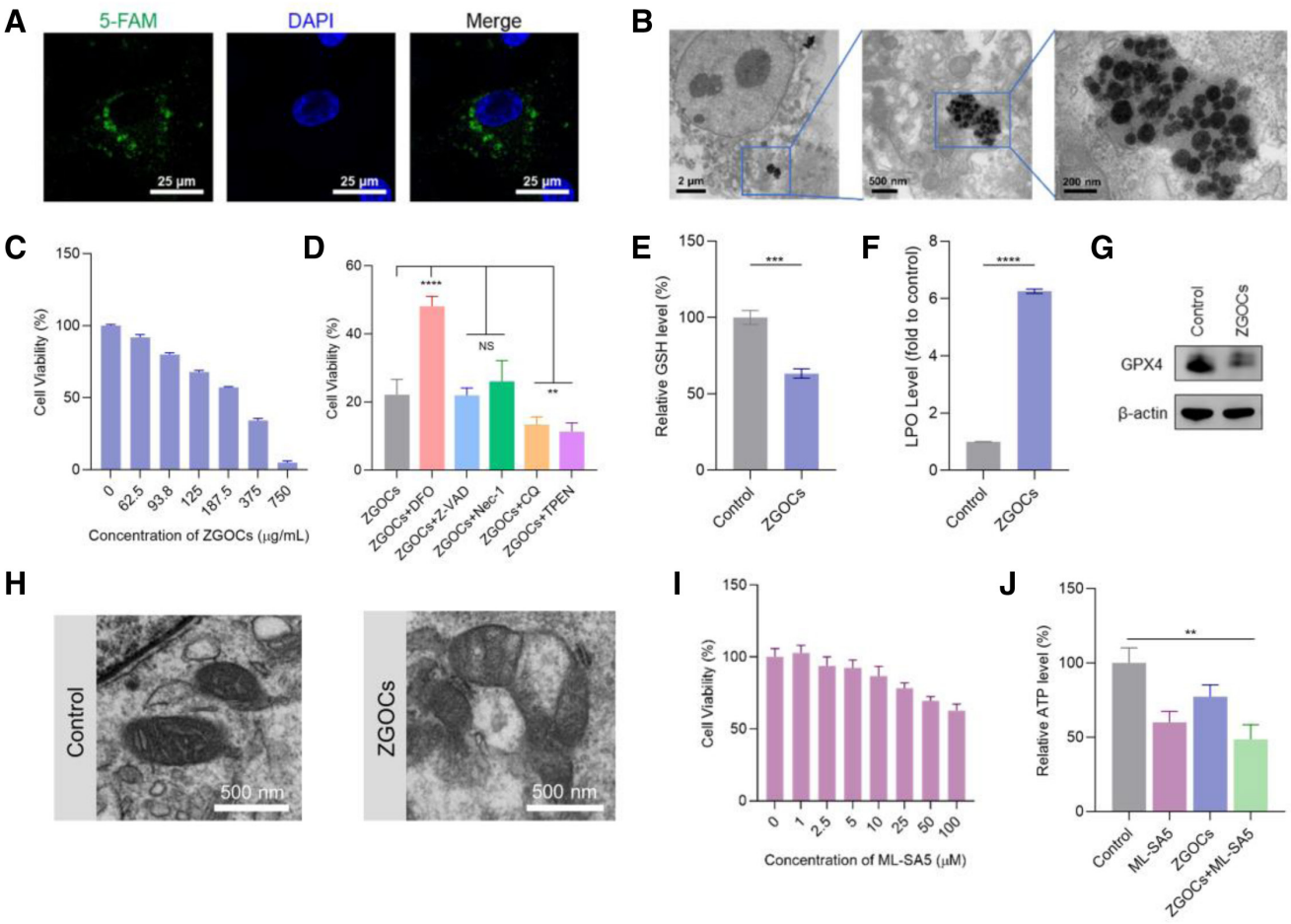

Figure 3. Antitumor effects and relative mechanism of ZGOCs. (A) CLSM images showing cellular uptake of 5-FAM-labeled ZGOCs in B16F10 cells, where blue represents cell nuclei, green represents NPs. (B) Bio-TEM images of B16F10 cells treated with ZGOCs. (C) Cell viability data of B16F10 cells when treated with ZGOCs at the indicated concentration for 24 h (n = 3). (D) Cell viability in B16F10 cells after being treated with ZGOCs with or without different cell death inhibitors (n = 3). The detection of (E) GSH levels (n = 3) and (F) LPO levels (n = 4) in B16F10 cells after ZGOCs treatments. (G) Western blot of GPX4 expression after ZGOCs treatments. (H) Bio-TEM images of the cross-sections of B16F10 cells after different treatments. (I) Cell viability of B16F10 cells treated with different concentrations of ML-SA5 for 24 h ($n \geq 3$). (J) Relative ATP of B16F10 cells after different treatments (n = 3). Data in (C–F) and (I–J) are presented as mean ± SD. P values: $^*P < 0.05$, $^{**}P < 0.01$, and $^{***}P < 0.001$, $^{****}P < 0.0001$. CLSM, confocal laser scanning microscopy; GPX4, glutathione peroxidase 4; GSH, glutathione; LPO, lipid peroxidation; NPs, nanoparticles; NS, no significance; TEM, transmission electron microscopy; ZGOCs, zinc gallate-based nanoclusters.

under ZGOCs treatments. The results showed that ZGOCs could strongly deplete GSH, and after treatment, GPX4 activity was significantly reduced (Figure 3E, G). The resulting GSH depletion and GPX4 inactivation further hindered the clearance of LPO (Figure 3F), indicating that ZGOCs could effectively suppress antioxidant defenses, thereby promoting ferroptosis.

To assess intracellular oxidative stress, we used 2,7-dichlorofluorescein diacetate (DCFH-DA) as a ROS probe. After 8 hours of ZGOCs treatment, a strong green fluorescence signal from DCF was observed in B16F10 cells, indicating elevated intracellular oxidative stress (Supplementary Figure S6, https://links.lww.com/MEDMAT/A7). Bio-TEM images also revealed that ZGOCs caused mitochondrial damage, as evidenced by the disruption of the mitochondrial cristae (Figure 3H).

Previous studies have shown that TRPML-specific synthetic agonists, such as ML-SA5 and ML-SA8, can induce rapid lysosomal Zn^{2+}-dependent necrotic cell death, termed lysozincrosis, in metastatic melanoma cells like M12 or MeWo[4]. Surprisingly, we found that ML-SA5 alone did not exhibit significant cytotoxicity in B16F10 cells, and only at high concentrations after 24 hours did it show a certain level of toxicity (Figure 3I). However, when ZGOCs (100 μg/mL) were combined with ML-SA5 (1 μM) in B16F10 cells, a potent antitumor effect was observed, which far exceeded the effects of either ZGOCs or ML-SA5 alone, accompanied by a significant reduction in intracellular ATP levels (Figure 3J and Supplementary Figure S7, https://links.lww.com/MEDMAT/A7). We hypothesized that this synergistic effect arose from Zn ions released by ZGOCs, which served as an exogenous Zn^{2+} source and, upon ML1 activation, cooperatively triggered lysozincrosis, thereby efficiently killing B16F10 cells.

3.3. In vivo *biodistribution and biocompatibility evaluation*

To facilitate the subsequent *in vivo* antitumor applications of ZGOCs, we next investigated their biodistribution and biosafety. Compared with Cy5.5-labeled free ZGO NPs (ZGO NPs/Cy5.5), Cy5.5-labeled ZGOCs (ZGOCs/Cy5.5) exhibited prolonged blood circulation time, suggesting their improved physiological stability and reduced rapid clearance by the body (Figure 4A–B). The prolonged circulation time of ZGOCs, together with their size more suitable for the enhanced permeability and retention effect, thereby favoring efficient tumor accumulation (Figure 4C)[26]. Moreover, as shown in Figure 4B, D, ZGOCs were predominantly metabolized through the liver and kidneys, which is consistent with the conventional metabolic pathways of NMs and indicates their feasibility for safe clearance from the body[26].

The biocompatibility of ZGOCs was further evaluated both *in vitro* and *in vivo*. Initially, different concentrations of ZGOCs were co-incubated with mouse erythrocytes, and no significant hemolysis (hemolysis ratio < 5%) or coagulation was observed compared with the control group, demonstrating excellent hemocompatibility (Figure 4E and Supplementary Figure S8, https://links.lww.com/MEDMAT/A7). Subsequently, *in vivo* safety assessments were carried out in female C57BL/6J mice. Specifically, mice received intravenous injections of either ZGOCs or saline (control) and were sacrificed on day 7 or 14 postinjection to evaluate both short-term and longer-term biosafety. Serum biochemistry and routine blood assays (Figure 4F–G and Supplementary Figure S9a, b, https://links.lww.com/MEDMAT/A7) revealed no significant differences in all tested parameters between the ZGOCs and control groups. In addition, H&E staining of major organs—including the heart, liver, spleen, lungs, and kidneys—revealed no pathological alterations or tissue damage at day 7 or 14 (Figure 4H and Supplementary Figure S9c, https://links.lww.com/MEDMAT/A7), further confirming the favorable short- and long-term safety profile of ZGOCs.

Taken together, these results confirmed that ZGOCs possessed favorable pharmacokinetics, efficient tumor-targeting capability, and excellent biocompatibility, highlighting their promise as a safe and effective nanoplatform for future melanoma therapy.

3.4. In vitro *and* in vivo *persistent luminescence performance*

We further investigated the *in vitro* and *in vivo* afterglow imaging performance of ZGO NPs due to their intrinsic PL capability. The excitation and emission spectra of ZGO NPs are shown in Figure 5A, B. Under UV excitation, ZGO NPs exhibited a broad emission band spanning the red to near-infrared (NIR) region (600–800 nm) with a pronounced peak at 695 nm. Interestingly, the formation of ZGO clusters (ZGOCs) resulted in an enhanced and prolonged PL intensity (Figure 5C), which can be ascribed to the effective suppression of surface defect–mediated nonradiative transitions within the densely packed cluster structure. In addition, the clustered configuration may partially shield the particles from water-induced quenching, thereby further sustaining the PL[19]. As shown in Figure 5E, following 10 min of UV excitation, ZGOCs displayed concentration-dependent afterglow performance, with the highest concentration group exhibiting decay times of approximately 20 min. Moreover, ZGOCs demonstrated rechargeable afterglow properties: upon re-excitation with UV light after initial decay, the afterglow intensity was fully restored without noticeable signal attenuation (Figure 5D and Supplementary Figure S10, https://links.lww.com/MEDMAT/A7).

The NIR emission of ZGOCs confers distinct advantages for *in vivo* applications, including deeper tissue penetration and minimized autofluorescence interference, which are critical for high-contrast imaging. Indeed, as illustrated in Figure 5F, in B16F10 tumor-bearing mice, intratumoral injection of ZGOCs enabled detectable afterglow within the tumor site for nearly 20 min, providing a sufficient imaging window for real-time tumor visualization and potential guidance for therapeutic interventions. Moreover, this afterglow can be reactivated on demand by subsequent UV excitation, demonstrating its rechargeable capability.

3.5. In vivo *synergistic anticancer evaluation*

Encouraged by the efficacy of ZGOCs in inducing metalloptosis and their biosafety, we conducted an *in vivo* therapeutic experiment to evaluate whether ZGOCs in combination with ML-SA5 could inhibit tumor growth. Subcutaneous melanoma models were established by inoculating B16F10 cells into C57BL/6J mice and allowing the tumors to grow for 7 days. The tumor-bearing mice were then randomly divided into 4 groups: saline (control), ML-SA5 alone, ZGOCs alone, and the combination of ZGOCs with ML-SA5. Following the treatment protocols shown in Figure 6A, it was evident that the tumor size in the "ZGOCs+ML-SA5" group was significantly smaller compared with the other groups (Figure 5B, C), indicating a more potent metalloptosis-inducing effect. The survival curves in Figure 5D further confirmed the synergistic effect of ZGOCs and ML-SA5. Throughout the treatment period, no significant weight loss was observed in the mice treated with ZGOCs, ML-SA5, or their combination, compared with the saline control group (Figure 5E). Consistent with the tumor inhibition results, H&E staining of tumor sections from the ZGOCs and ML-SA5 combination group showed distinct features of necrotic cells, such as cell shrinkage, loss of cell–cell contacts, and condensed chromatin (Figure 5F). Moreover, IHC of Ki-67, a marker of cell proliferation, and xCT, a key cystine/glutamate antiporter that suppresses ferroptosis, further confirmed that the combination treatment induced the most pronounced inhibition of tumor growth and activation of ferroptosis (Supplementary Figure

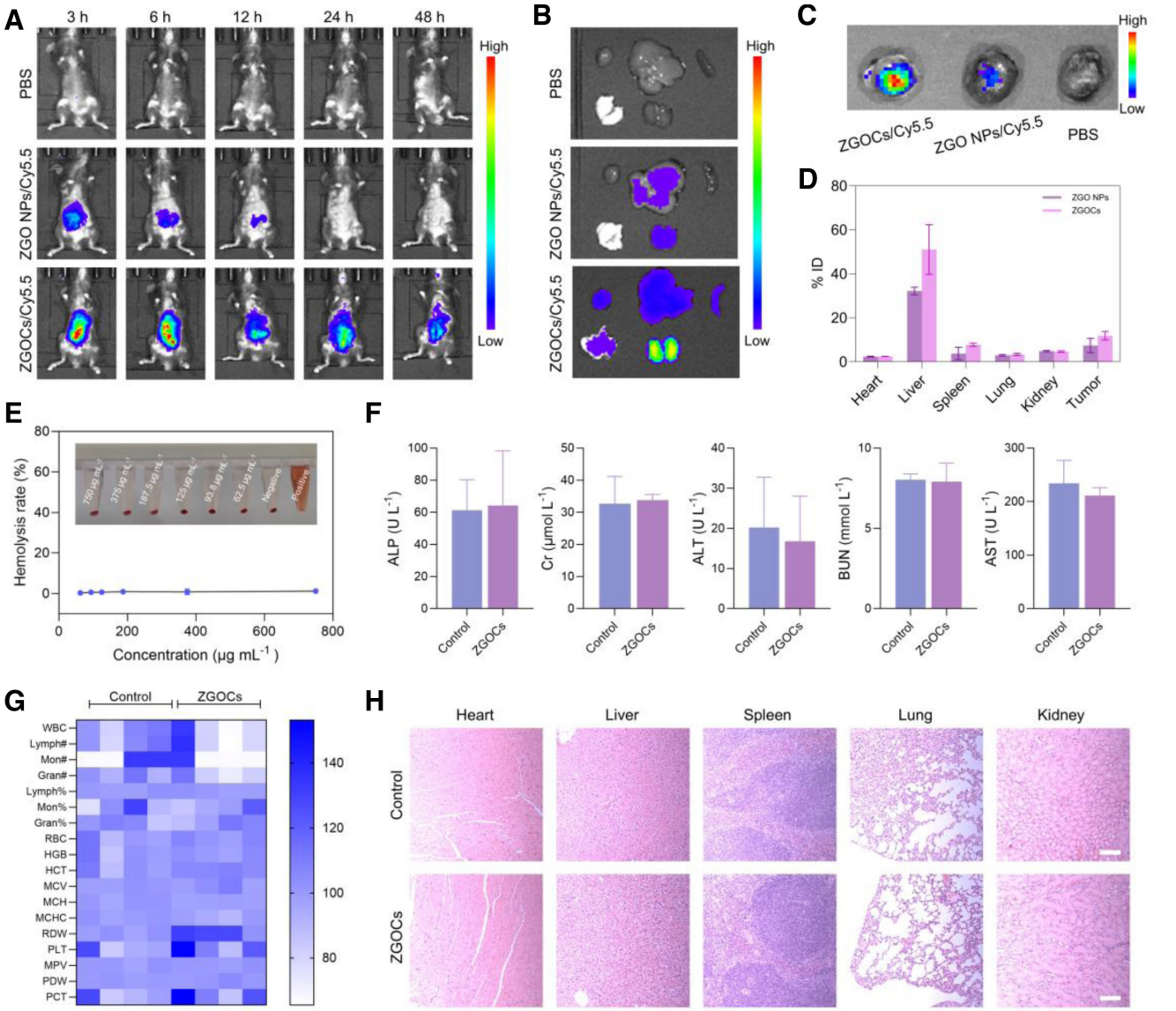

Figure 4. Biodistribution and biocompatibility assessment of ZGOCs. (A) Fluorescence images at the indicated time of tumor-bearing mice after intravenous injection with PBS, ZGO NPs, and ZGOCs. (B, C) Representative in vivo fluorescence images of (B) major organs and (C) tumors at 48 h after treatment of different treatment groups. (D) Biodistribution of ZGO NPs or ZGOCs in tumor-bearing mice after 48 hours postinjection. (E) Hemolysis assay of ZGOCs at different concentrations. Saline was set as the negative control, and distilled water was set as the positive control. (F) Serum biochemistry analysis (n = 3), (G) routine blood assay (n = 4), and (H) H&E staining images of major organs from mice treated with saline (control) and ZGOCs for 7 days. Scale bar: 200 μm. Data in (D–F) are presented as mean ± SD. H&E, hematoxylin and eosin; NPs, nanoparticles; ZGO, $ZnGa_2O_4$; ZGOCs, zinc gallate-based nanoclusters.

S11, https://links.lww.com/MEDMAT/A7). Overall, the synergistic action of ZGOCs and ML-SA5 effectively induced metalloptosis in melanoma-bearing mice, leading to significant tumor suppression and achieving a favorable therapeutic outcome.

4. Conclusions

For an enhanced metalloptosis strategy disrupting ion homeostasis in metastatic melanoma, ZGOCs combining with ML-SA5 were successfully developed for the treatment of melanoma. The synthesized ZGOCs exhibited uniform morphology, good stability, and strong metalloptosis-inducing capabilities. These nanoclusters were responsive to the acidic TME, where they degraded to release gallium and Zn ions. On one hand, these metal ions triggered GSH depletion, ROS production, and GPX4 deactivation in B16F10 cells, ultimately leading to a sharp increase in LPO levels for inducing ferroptosis. On the other hand, the released Zn ions synergized with ML-SA5, a TRPML1 agonist, to potentiate lysozincrosis, ultimately enhancing melanoma cell death. This dual pathway of ferroptosis and lysozincrosis was further validated *in vivo*, where the combination of ZGOCs and ML-SA5 effectively suppressed tumor growth with favorable biosafety.

In parallel, the unique optical properties of ZGOCs provided additional diagnostic advantages. Unlike conventional fluorescent probes that require continuous external excitation, ZGOCs exhibited long-lasting, rechargeable afterglow emission. The cluster formation further suppressed nonradiative transitions, thereby prolonging the duration and intensity of the afterglow. Importantly, the emission lies in the NIR window, which matches well with the superficial growth characteristics of melanoma, enabling deeper tissue penetration, minimized autofluorescence, and real-time tumor tracking. These features highlight ZGOCs as a dual-functional platform that integrates therapeutic efficacy with high-contrast afterglow imaging, thereby advancing precise melanoma theranostics.

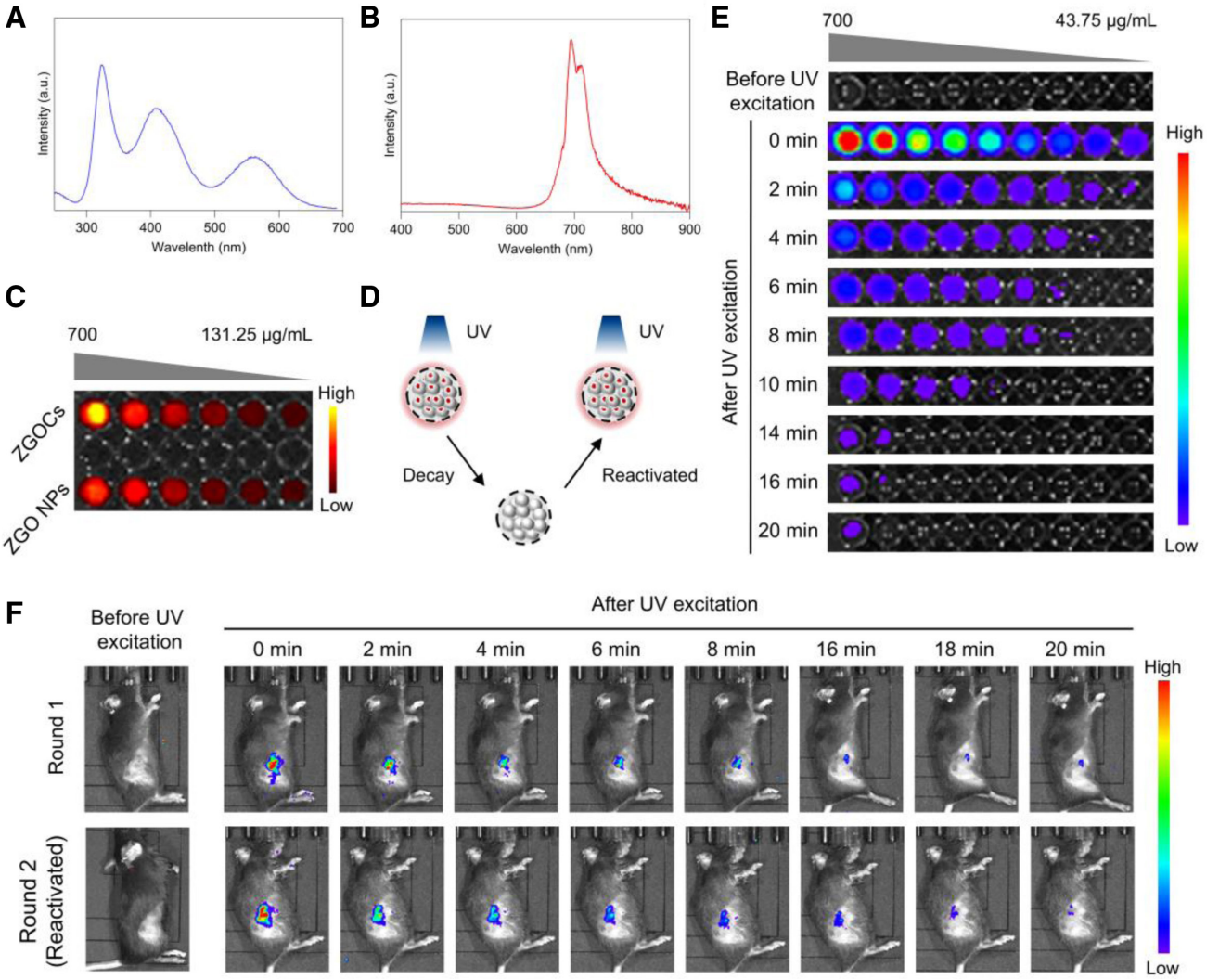

Figure 5. In vitro and in vivo afterglow imaging performance of ZGO NPs and ZGOCs. (A) Excitation spectrum of ZGO NPs by monitoring the Cr^{3+} emission at 695 nm. (B) Emission spectrum of ZGO NPs under UV excitation at 260 nm. (C) PL images of ZGO NPs and ZGOCs after UV excitation at different concentrations. (D) Schematic illustration showing the rechargeable and UV-activated PL in ZGOCs. (E) Luminescence images of ZGOCs solution at different concentrations, recorded at various time points after excitation. (F) Luminescence images of tumor-bearing mice after intratumoral injection of ZGOCs, recorded at various time points postexcitation and reactivated. NPs, nanoparticles; PL, persistent luminescence; ZGO, $ZnGa_2O_4$; ZGOCs, zinc gallate-based nanoclusters.

It is also worth noting that this clustering strategy is not limited to single ZGO-based systems. ZGO NPs could also be hybridized with other functional NMs, such as gold or iron carbide (Fe_2C) NPs, further expanding the bio-application range of this strategy (Supplementary Figure S12, https://links.lww.com/MEDMAT/A7). For example, integrating gold or Fe_2C NPs may endow the hybrid clusters with strong photothermal or magnetothermal conversion efficiency, thereby enabling synergistic thermal ablation in combination with metalloptosis. In parallel, the incorporation of these functional components also enhances diagnostic capabilities—gold NPs can serve as excellent computed tomography contrast agents, while Fe_2C NPs offers magnetic resonance imaging potential—supporting multimodal imaging-guided therapy.

Acknowledgements

This work was financially supported by the National Natural Science Foundation of China (Grant Nos. 52201198, 22575006, 52027801, and 92263203), Beijing Natural Science Foundation-Haidian Primitive Innovation Joint Fund (Grant No. L232015), the National Key R&D Program of China (Grant No. 2022YFA1203902), the China-Germany Collaboration Project (Grant No. M-0199), the Fundamental Research Funds for the Central Universities, Peking University, The Clinical Medicine Plus X-Young Scholars Project of Peking University, and the Fundamental Research Funds for the Central Universities (Grant Nos. PKU2024LCXQ014 and PKU2025PKULCXQ040).

Conflicts of interest

The authors declare that they have no conflicts of interest.

Data availability statement

The data that support the findings of this study are available from the corresponding author upon reasonable request.

Author Contribution

Shuren Wang supervised and administered the project. Yanglong Hou, Shuren Wang, and Ran Ma conceived and designed the experiments. Ran Ma, Jiajia Liu, and Zi Mei performed the ex-

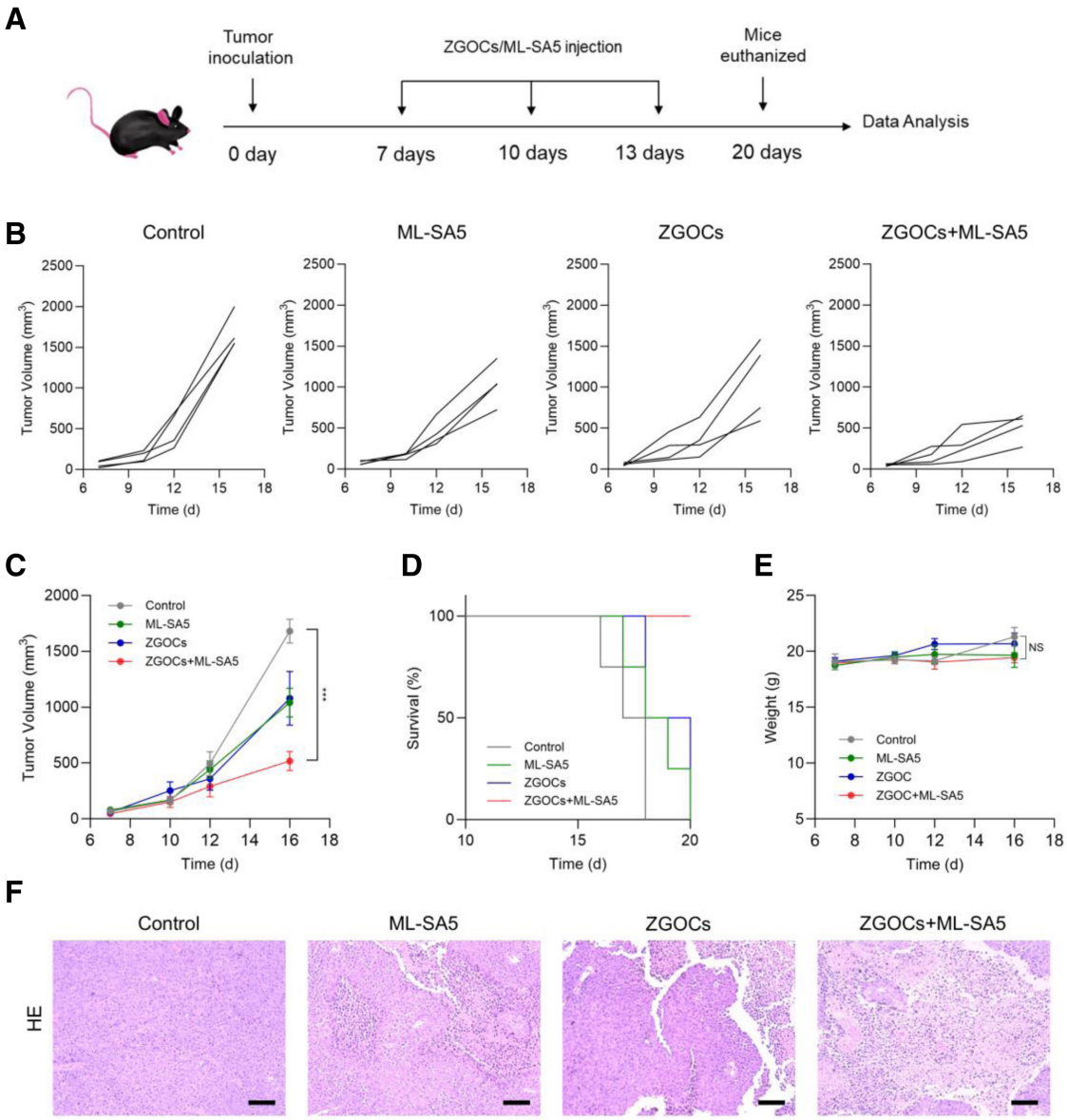

Figure 6. In vivo therapeutic effect of ZGOCs. (A) Schematic treatment protocol of the mice with different treatments (n = 4). (B) Individual tumor growth curves, (C) average tumor growth curves, and (D) survival rate of mice after different treatments (n = 4). (E) Body weight of tumor-bearing mice under various treatments (n = 4). (F) H&E staining images of tumor tissues at the end of various treatments. Scale bar: 200 μm. Data in (C, E) are presented as mean ± SEM. P values: $^{*}P < 0.05$, $^{**}P < 0.01$, and $^{***}P < 0.001$. H&E, hematoxylin and eosin; NS, not significant; ZGOCs, zinc gallate-based nanoclusters.

periments, collected the data, analyzed, and interpreted the data. Ran Ma and Shuren Wang wrote the paper. All the authors discussed the results and reviewed the paper at all stages.

References

[1] Welsh SJ, Rizos H, Scolyer RA, et al. Resistance to combination BRAF and MEK inhibition in metastatic melanoma: where to next? *Eur J Cancer (Oxford, England: 1990)*. 2016;62:76–85.

[2] Kasitinon SY, Eskiocak U, Martin M, et al. TRPML1 promotes protein homeostasis in melanoma cells by negatively regulating MAPK and mTORC1 signaling. *Cell Rep*. 2019;28(9):2293–2305.e9.

[3] Dong X-P, Cheng X, Mills E, et al. The type IV mucolipidosis-associated protein TRPML1 is an endolysosomal iron release channel. *Nature*. 2008;455(7215):992–996.

[4] Du W, Gu M, Hu M, et al. Lysosomal Zn^{2+} release triggers rapid, mitochondria-mediated, non-apoptotic cell death in metastatic melanoma. *Cell Rep*. 2021;37(3):109848.

[5] Bakhshi J, Weinstein L, Poksay KS, et al. Coupling endoplasmic reticulum stress to the cell death program in mouse melanoma cells: effect of curcumin. *Apoptosis*. 2008;13(7):904–914.

[6] Xu L, Peng M, Gao T, et al. Nanoenabled intracellular metal ion homeostasis regulation for tumor therapy. *Adv Sci*. 2024;11(7):e2306203.

[7] Ma R, Hou Y, Wang S. Combatting cancer with tiny intelligent warriors: Stimuli-responsive micro/nanorobots in chemotherapeutic delivery. *Sci China Mater*. 2024;67(8):2469–2476.

[8] Ma R, Hou Y, Wang S. Imaging-guided cancer therapy based on multifunctional magnetic nanoparticles. *Chin J Chem*. 2023;41(19):2557–2573.

[9] Wang S, Wang Z, Li Z, et al. Amelioration of systemic antitumor immune responses in cocktail therapy by immunomodulatory nanozymes. *Sci Adv*. 2022;8(21):eabn3883.

[10] Wang J, Sun Z, Wang S, et al. Biodegradable ferrous sulfide-based nanocomposites for tumor theranostics through specific intratumoral acidosis-induced metabolic symbiosis disruption. *J Am Chem Soc*. 2022;144(43):19884–19895.

[11] Wang S, Ma R, Mei Z, et al. Metalloptosis: metal ions-induced programmed cell death based on nanomaterials for cancer therapy. *MedMat*. 2024;1(1):6–26.

[12] Ko MJ, Min S, Hong H, et al. Magnetic nanoparticles for ferroptosis cancer therapy with diagnostic imaging. *Bioact Mater*. 2024;32:66–97.
[13] Gu J, Guo C, Ruan J, et al. From ferroptosis to cuproptosis, and calcicoptosis, to find more novel metals-mediated distinct form of regulated cell death. *Apoptosis*. 2024;29(5):586–604.
[14] Wang J, Zhang R, Gao S, et al. Degradable nanoregulators based on ultra-small ferrous sulfide for photoacoustic/magnetic resonance imaging-guided tumor starvation and ferroptosis. *Adv Healthc Mater*. 2025;14(19):e2500560.
[15] Wang J, Fang Z, Zhao C, et al. Intelligent size-switchable iron carbide-based nanocapsules with cascade delivery capacity for hyperthermia-enhanced deep tumor ferroptosis. *Adv Mater*. 2024;36(9):e2307006.
[16] Dixon SJ, Lemberg KM, Lamprecht MR, et al. Ferroptosis: an iron-dependent form of nonapoptotic cell death. *Cell*. 2012;149(5):1060–1072.
[17] Lei G, Zhuang L, Gan B. Targeting ferroptosis as a vulnerability in cancer. *Nat Rev Cancer*. 2022;22(7):381–396.
[18] Shen Z, Song J, Yung BC, et al. Emerging strategies of cancer therapy based on ferroptosis. *Adv Mater*. 2018;30(12):e1704007.
[19] Fan W, Lu N, Xu C, et al. Enhanced afterglow performance of persistent luminescence implants for efficient repeatable photodynamic therapy. *ACS Nano*. 2017;11(6):5864–5872.
[20] Davis ME, Chen Z, Shin DM. Nanoparticle therapeutics: an emerging treatment modality for cancer. *Nat Rev Drug Discovery*. 2008;7(9):771–782.
[21] Bai F, Wang D, Huo Z, et al. A versatile bottom-up assembly approach to colloidal spheres from nanocrystals. *Angew Chem Int Ed*. 2007;46(35):6650–6653.
[22] Wang S, Ma K, Chen L, et al. TAZ promotes cell growth and inhibits celastrol-induced cell apoptosis. *Biosci Rep*. 2016;36(5):e00386.
[23] Blanco E, Shen H, Ferrari M. Principles of nanoparticle design for overcoming biological barriers to drug delivery. *Nat Biotechnol*. 2015;33(9):941–951.
[24] Zhou Z, Zheng W, Kong J, et al. Rechargeable and LED-activated ZnGa2O4: Cr3+ near-infrared persistent luminescence nanoprobes for background-free biodetection. 10.1039/C7NR01209H. *Nanoscale*. 2017;9(20):6846–6853.
[25] Peng X-X, Zhang H, Zhang R, et al. Gallium triggers ferroptosis through a synergistic mechanism. *Angew Chem Int Ed*. 2023;62(36):e202307838.
[26] Xu M, Qi Y, Liu G, et al. Size-dependent in vivo transport of nanoparticles: implications for delivery, targeting, and clearance. *ACS Nano*. 2023;17(21):20825–20849.

How to cite this article: Ma R, Liu J, Mei Z, Hou Y, Wang S. Zinc gallate nanoclusters-mediated enhanced metalloptosis in melanoma. MedMat 2026;3(2):e00034. doi: 10.1097/mm9.0000000000000034